Mixing between chemically variable primitive basalts creates and modifies crystal cargoes

David A. Neave[1,2]*, Philipp Beckmann[2], Harald Behrens[2] and François Holtz[2]

[1]Department of Earth and Environmental Sciences, The University of Manchester, Manchester, UK

[2]Leibniz Universität Hannover, Institut für Mineralogie, Hannover, Germany

*Email: david.neave@manchester.ac.uk

Revised manuscript for submission to Nature Communications.

Abstract (149/150 words) Main text (4998/5000 words) Methods (1397/3000 words) Figures (10/10)

Abstract

Basaltic crystal cargoes often preserve records of mantle-derived chemical variability that have been erased from their carrier liquids by magma mixing. However, the consequences of mixing between similarly primitive but otherwise chemically variable magmas remain poorly understood despite ubiquitous evidence of chemical variability in primary melt compositions and mixing-induced disequilibrium within erupted crystal cargoes. Here we report observations from magma-magma reaction experiments performed on analogues of primitive Icelandic lavas derived from distinct mantle sources to determine how their crystal cargoes respond to mixing-induced chemical disequilibrium. Chemical variability in our experimental products is controlled dominantly by major element diffusion in the melt that alters phase equilibria and triggers plagioclase resorption within regions that were initially plagioclase saturated. Isothermal mixing between chemically variable basaltic magmas may therefore play important but previously underappreciated roles in creating and modifying crystal cargoes by unlocking plagioclase-rich mushes and driving resorption, (re-)crystallisation and solid-state diffusion.

Chemical variability in primitive mid-ocean ridge and ocean island basalts (MORB and OIB, respectively; oceanic basalts, collectively) results from variability in mantle melting processes and source compositions[1,2]. Correlations between the isotopic and incompatible-element compositions of erupted basalts reflect how the subduction and subsequent in-mixing of oceanic lithosphere by mantle convection have created deep isotopic and chemical heterogeneities through geological time[3]. Subduction has also created deep lithological heterogeneities that propagate into correlated variations in the major and trace element compositions of erupted basalts[4,5]. Thus, similarly primitive but otherwise chemically variable oceanic basalts have different phase equilibria at the same pressure–temperature (*P*–*T*) conditions and consequently evolve along compositionally distinct trajectories[6,7]. However, mantle-derived chemical variability is progressively erased by mixing during magma ascent and evolution[8,9], meaning that erupted basalts are typically less diverse than the primary melts from which they have evolved[10]. Fortunately, vital records of mantle-derived chemical variability are often preserved within crystals and melt inclusions that are typically more resistant to mixing-induced re-equilibration than their carrier liquids[11–15]. Nevertheless, surprisingly little is known about crystal-melt interactions taking place during mixing between chemically variable oceanic basalts and their roles in creating and modifying crystal cargoes.

Records of mantle-derived variability in basaltic crystal cargoes are associated with disequilibrium features that range from simple normal zoning to complex textures reflecting resorption, rapid crystal growth and diffusive re-equilibration[16–18]. Crystal-hosted melt inclusions provide complementary archives that confirm the presence of mantle-derived chemical variability within individual magma plumbing systems[13,14]. Indeed, this chemical variability may play a fundamental role in creating some types of melt inclusion[19,20]. Disequilibrium features in crystal cargoes record changes in magma *P*–*T*–H_2O activity (a_{H_2O})–oxygen fugacity (f_{O_2})–composition (*X*) conditions as well as the timescales over which these changes occur. For example, compositional zoning in plagioclase crystals often preserves information about magma reservoir processes and transport pathways[21–23], while compositional zoning in olivine crystals often records timescales of magma storage and ascent[24–26]. Although recharge by hot and primitive magmas is a long-recognised

mechanism for creating disequilibrium features within crystal cargoes[17,18,27], near-isothermal mixing between chemically variable magmas is also likely to have important but as yet ill-defined impacts.

Experimental simulations of magma mixing typically focus on physical mingling in dynamic experiments[28–32] or diffusive re-equilibration in classic melt-melt couples[33,34]. While physical mingling is an essential component of magma mixing, diffusion over short (i.e. μm) lengthscales ultimately changes local melt compositions and leads to the modification of crystals by resorption, (re-)crystallisation and solid-state diffusion. However, melt-melt couple experiments are, by definition, performed under superliquidus conditions and thus provide limited insights into magma-magma reactions[33,35]. Although constitutional undercooling and diffusive controls over crystal growth and resorption have been investigated in some simple systems[36–40], and crystal-bearing mixing experiments have been performed in the contexts of enclave formation and andesite formation by magma hybridisation[32,41], current observations typically constrain how pressure and temperature affect mineral stabilities rather than melt composition.

Mantle-derived chemical variability is especially well characterised in basalts from southwest Iceland. At any given MgO content, incompatible element-depleted basalts from lherzolitic mantle sources are rich in Al_2O_3 and CaO but poor in FeO* (total Fe expressed as FeO) and Na_2O , while incompatible element-enriched basalts from recycled mantle sources are poor in Al_2O_3 and CaO but rich in FeO* and Na_2O[42]. This dichotomy is exemplified by the Háleyjabunga and Stapafell lavas on the Reykjanes Peninsula (Figs. 1a, 1b)[13]. Crystallisation experiments performed on synthetic analogues of these lavas illustrate how mantle-derived variability in major element compositions affects their phase equilibria[7]. Namely, plagioclase crystallises at >1200 °C from the Al_2O_3-rich and incompatible element-depleted Háleyjabunga lava analogue but only at <1180 °C from the Al_2O_3-poor and incompatible element-enriched Stapafell lava analogue (Figs. 1c, 1d). For any given decrease in temperature, incompatible element-depleted magmas thus crystallise a greater proportion of their mass than their incompatible element-enriched counterparts, potentially resulting in the deep sequestration of incompatible element-depleted magmas as plagioclase-rich cumulates and the progressive biasing of evolved magmas towards incompatible element-enriched compositions[7].

Here we present the results of magma-magma reaction experiments designed to determine how mixing-induced chemical disequilibrium affects the crystal cargoes of chemically variable oceanic basalts. We did this by juxtaposing synthetic magma analogues of the Háleyjabunga and Stapafell lavas at 300 MPa and 1190 °C for durations of 1 to 96 hours under realistic magma storage conditions – 300 MPa, 1190 °C, low water activities (~0.06) and oxygen fugacities approximately one log unit above the fayalite-magnetite-quartz buffer (full details are provided in the methods)[7,43]. We first examine phase relations across juxtaposed magma analogues and describe how crystals responded to the diffusive re-equilibration of melt major element contents between initially distinct magmas. We then explore the implications of our findings for the creation and modification of basaltic crystal cargoes by magma mixing and mush disaggregation.

Results

Magma synthesis experiments. The products of synthesis experiments performed on the incompatible element-depleted Háleyjabunga lava analogue and incompatible element-enriched Stapafell lava analogue contain crystals of olivine, clinopyroxene and plagioclase (Fig. 2a, 2c), and olivine and clinopyroxene (Fig. 2b, 2d), respectively. Although the products of the experiment on the Stapafell analogue have a lower glass content (i.e. melt mass fraction, F) than those of the experiment on the Háleyjabunga analogue (F = 0.72 and 0.90, respectively, according to mass balance; Supplementary Data), glasses are interconnected throughout the products of both synthesis experiments. Crystals are typically euhedral to subhedral, though some plagioclase crystals are skeletal and contain melt inclusions. While clinopyroxene crystals sometimes form aggregates, degrees of crystal impingement are generally low. Some olivine crystals contain small inclusions of plagioclase (Fig. 2d).

Magma-magma reaction experiments. The products of magma-magma reaction experiments share textural and mineralogical characteristics with products of magma synthesis experiments (Figs. 3, 4). Namely, crystals are smaller and more abundant in products derived from the incompatible element-depleted Háleyjabunga analogue than those from the incompatible element-enriched Stapafell

105 analogue. Overall, textures of crystals far from original interfaces do not appear to evolve with
106 increasing experimental duration; only clinopyroxene crystals in portions of experimental products
107 derived from the Stapafell analogue show possible evidence of Ostwald ripening (Fig. 4d). Although
108 crystal fractions remain broadly constant with increasing experimental duration in far-field portions of
109 experimental products derived from the Háleyjabunga analogue away from initial magma-magma
110 interfaces (Figs. 3, 4a, 4b), they appear to decrease in those derived from the Stapafell analogue (Figs.
111 3, 4c, 4d). However, mass balance demonstrates that far-field melt mass fractions change little
112 through time: between 1 and 96 hours, *F* changes from 0.77 to 0.80 in far-field portions of the
113 Háleyjabunga analogue, and 0.92 to 0.93 in far-field portions of the Stapafell analogue. It is therefore
114 likely that apparent differences in observed crystal fractions are related to heterogeneities created by
115 gravitational settling during the synthesis experiment on the Stapafell analogue and that
116 disequilibrium crystal fractions were retained through magma-magma reaction experiments.
117 Somewhat lower crystal fractions in the products of magma-magma reaction experiments with respect
118 to the products of synthesis experiments reflect samples of the latter being sourced from capsule ends
119 that lay slightly outside the vessel's hot zone.

120 Glass composition profiles through the products of magma-magma reaction experiments have
121 variably linear and sigmoidal forms that depend on both experimental duration and the element in
122 question (Fig. 5). Profiles near the central axes of experimental products have similar forms to those
123 near capsule walls, meaning that parallel profiles could be stacked on their common midpoints.
124 Importantly, the similarity of parallel profiles demonstrates that advection was negligible once
125 magma-magma interfaces were established (early advection is reflected in curved magma-magma
126 interfaces in the products of 1- and 4-hour experiments) and that experimental products record
127 dominantly diffusive signals.

128 Far-field glasses derived from the Stapafell analogue have lower Al_2O_3 contents and higher
129 FeO*, TiO_2 and K_2O contents than those derived from the Háleyjabunga analogue after short
130 experimental durations of 1 and 4 hours (~14.5 versus ~16.0 wt.% for Al_2O_3, ~11.0 versus ~10.0 wt.%
131 for FeO*, ~1.65 versus ~0.75 wt.% for TiO_2 and ~0.22 versus ~0.10 wt.% for K_2O, respectively;

Figs. 5a–c, 5e). Differences in far-field Al_2O_3 and TiO_2 contents remain clear after longer experimental durations of 24 and 96 hours while those in FeO* and K_2O contents are muted or overprinted. Differences in CaO and Na_2O contents are visible after 1 and 4 hours (~12.0 versus ~12.6 wt.% for CaO and ~2.1 versus ~1.7 wt.% for Na_2O, respectively; Figs. 5d, 5f) but challenging to distinguish from analytical uncertainty after 24 and 96 hours (2σ = ±0.44 wt.% and ±1.3 wt.% for CaO and Na_2O, respectively). Small differences in MgO contents (~8.3 versus ~8.5 wt.%) also cannot be observed after 4 hours (Fig. 5g); the slightly higher MgO content of products from magma-magma reaction experiments with respect to synthesis experiments is consistent with the latter having equilibrated slightly outside the vessel's hot zone.

Al_2O_3 TiO_2 and K_2O profiles have sigmoidal forms that show progressively more gradual transitions between far-field compositions with increasing experimental durations (Figs. 5a, 5c, 5e). FeO* profiles are sigmoidal in the products of 1- and 4-hour experiments, but near-linear in the products of 24- and 96-hour experiments (Fig. 5b). FeO* contents are also displaced to lower mean FeO* contents in the products of the 24- and 96-hour experiments with respect those of the 1- and 4-hour experiments. Mass balance indicates that this results from modest Fe loss from $Au_{80}Pd_{20}$ capsules in the case of former (1–2 % relative) and modest Fe gain in the case of the latter (2–5 wt.% relative)[44]. CaO and Na_2O profiles are sigmoidal in the products of 1- and 4-hour experiments, but linear in the products of 24- and 96-hour experiments, (Figs. 5d, 5f).

Diffusive re-equilibration of experimental glasses. Normalising distances through experimental products by the square root of experimental duration demonstrates that glass compositions are primarily controlled by diffusive re-equilibration between chemically distinct melts in the starting magma analogues[34,45] – Al_2O and TiO_2 profiles are shown in Fig. 6. This is because diffusion distance scales with the square root of the diffusion coefficient multiplied by diffusion time (i.e. $x \propto \sqrt{Dt}$, where x is the diffusion distance, D is the diffusion coefficient and t is time)[45], meaning that diffusively controlled composition profiles stack once time is cancelled out[34]. Overlapping profiles in Fig. 6 demonstrate that diffusion operated coherently throughout our magma-magma reaction experiments and that observations can be integrated across our different experiments.

Effective binary diffusion coefficients estimated by fitting error functions through glass composition profiles to solve Fick's 2nd Law are consistent with the modest body of published values available (Fig. 7)[35–38,46–49]. Most published diffusion coefficients for basaltic melts have been derived from crystal dissolution experiments[36–38] or classic melt-melt couples[35,46]. Na diffusivity has also been estimated from radiotracer diffusion experiments[47]. Where error functions could be fitted to our glass composition profiles by assuming that melt viscosity does not vary across experimental products (Supplementary Material), estimated effective binary diffusion coefficients are typically within one ln unit of regressions through published datasets that follow Arrhenian relationships ($D = D_0 e^{-E_A/RT}$, where D is the diffusion coefficient, D_0 is the pre-exponential factor, E_A is the activation energy for diffusion and R is the gas constant; Fig. 7).

Diffusion coefficients estimated from our 1- and 4-hour experiments are particularly close to global regressions for Al_2O_3, FeO* and CaO (r^2 = 0.83, 0.92 and 0.79 respectively), suggesting that the behaviour of these elements in basaltic melts can be largely explained without complex multicomponent diffusion models (Figs. 7a, 7b, 7d). While our estimated diffusion coefficients for TiO_2 are similar to published values, the latter span three ln units at any given T and global regression statistics are modest (r^2 = 0.59), suggesting that TiO_2 may diffuse by a different mechanism from Al_2O_3, FeO* and CaO, at least when present a relatively low concentrations (Fig. 7c). Although published diffusion coefficients are scarce for K_2O and Na_2O[46,47], our estimates fall on plausibly Arrhenian trends with the few data available (Fig. 7e, 7f). Estimated diffusivities of Al_2O_3 and TiO_2 are similar to theoretical Eyring diffusivities ($D_E = k_B T/\lambda\eta$, where D_E is the Eyring diffusivity, k_B is Boltzmann's constant, λ is a jump distance of 0.4 nm related to the atomic spacing of silicate liquids and η is the average viscosity of the two end-member melts (12.5 Pa.s), calculated here with the model of Giordano et al.[50])[51]; Eyring diffusivities are typically good at describing the behaviour of relatively high-field strength network-forming cations (i.e. Si, Al and Ti) and oxygen[34]. In contrast, estimated diffusivities of lower-field strength Na_2O and K_2O are higher, reflecting variable degrees of decoupling from network-forming cations (Figs. 7e, 7f)[52,53]. Finally, we note that melt H_2O contents were not reported in the published data considered here, and that small variations in melt H_2O

contents (~1 wt.%) affect the diffusivity of network-forming and high-field strength elements considerably[45].

Mineral stabilities and compositions. Olivine crystals occur in the products of magma synthesis experiments on both lava analogues (Figs. 2, 8a). However, they have slightly higher forsterite contents [X_{Fo} ~ 0.852 versus 0.843, respectively, where X_{Fo} = Mg/(Mg+Fe) on a molar basis] in the products of the experiment on the FeO*-poor Háleyjabunga analogue than those of the experiment on the FeO*-rich Stapafell analogue. This difference is reflected in steps in mean X_{Fo} across magma-magma interfaces in the products of 1- and 4-hour experiments (Fig. 8a). Unfortunately, the abundance of olivine crystals is insufficient to determine whether these X_{Fo} steps persist in the products of 24- and 96-hour experiments. Some olivine crystals from longer duration experiments show evidence of diffusive re-equilibration in response to Fe loss (higher X_{Fo} contents than in the products of synthesis or shorter duration experiments) and diffusive homogenisation of melt FeO* contents (X_{Fo} variance decreases from 2.9×10^{-5} after 1 hour to 9.6×10^{-6} after 96 hours). Indeed, olivine crystals in the products of the 24-hour experiment appear to show diffusion profiles that are absent from the products of shorter experiments (Supplementary Fig. 1).

Plagioclase crystals occur in the products of the synthesis experiment on the Háleyjabunga analogue but not the Stapafell analogue (Figs. 2, 8b). Plagioclase is also only stable within the portions of magma-magma reaction experiments initially derived from the Háleyjabunga lava analogue. In line with published phase equilibria[7], plagioclase crystals have uniformly high anorthite contents [X_{An} ~ 0.83, where X_{An} = Ca/(Ca+Na+K) on a molar basis]. Although X_{An} variability exceeds analytical uncertainty in the products of all magma-magma reaction experiments (Fig. 8b), likely because of rapid crystal growth that is also reflected in skeletal textures (Figs. 2, 4)[54], mean X_{An} does not vary systematically as a function of either position or experimental duration. Plagioclase stability, on the other hand, depends strongly on experimental duration. While plagioclase is stable throughout the portion of the 1-hour experiment derived from the synthesis experiment on the Háleyjabunga lava analogue (Fig. 3a), regions where plagioclase is stable progressively shrink as experimental duration increases (Figs. 3b–d), leaving >1-mm broad regions of plagioclase resorption in the products of 24-

and 96-hour experiments. Projecting regions of plagioclase stability onto time-normalised composition profiles indicates that plagioclase resorption occurs when melt Al_2O_3 contents decrease below ~16 wt.% by diffusive re-equilibration within the melt (Fig. 6a). The region of plagioclase stability in the products of 24-hour experiments is smaller than expected from comparisons with the products of other experiments, which we attribute to the modification of melt compositions by Fe loss to capsule materials leading to corresponding increases in other components including Al_2O_3. Nevertheless, our experiments indicate that plagioclase stability is dominantly controlled by melt Al_2O_3 content rather than melt CaO and Na_2O contents (or melt Ca/Na) as both CaO and Na_2O diffuse considerably faster than Al_2O_3 (Fig. 7)[48].

Clinopyroxene crystals occur in the products of synthesis experiments on both lava analogues (Fig. 2). While much variability in clinopyroxene Mg-number [$Mg\#_{cpx}$, where $Mg\#_{cpx}$ = Mg/(Mg+Fe) on a molar basis] is related to sector zoning[55], a slight difference in mean $Mg\#_{cpx}$ between the products of the experiments on the Háleyjabunga and Stapafell analogues (0.835 versus 0.850, respectively) reflects differences in their melt FeO* contents (Fig. 8c). However, differences between the two magma analogues are more clearly expressed in terms of mean clinopyroxene TiO_2 contents, with clinopyroxene crystals grown from the incompatible element-enriched Stapafell analogue containing considerably more TiO_2 than those grown from the incompatible element-depleted Háleyjabunga analogue (~0.48 versus ~0.28 wt.%, respectively; Fig. 8d). Chemical variability associated with clinopyroxene sector zoning masks $Mg\#_{cpx}$ steps across magma-magma interfaces in the products of magma-magma reaction experiments (steps of ~0.01 are difficult to resolve within total $Mg\#_{cpx}$ ranges of 0.825–0.855, Fig. 8c). Nevertheless, overall gradients of low $Mg\#_{cpx}$ in the Stapafell analogue increasing to high $Mg\#_{cpx}$ in the Háleyjabunga analogue can still be discerned. Steps in clinopyroxene TiO_2 contents between magma analogues are much more distinct (from ~0.2–0.3 wt.% in portions derived from the Háleyjabunga analogue to 0.4–0.6 wt.% in portions derived from the Stapafell analogue; Fig. 8d), consistent with the slow intra-crystalline diffusion of TiO_2 during our experiments[56]. Positions of TiO_2 steps do, however, vary with experimental duration, with high-TiO_2 clinopyroxene crystals seemingly replacing low-TiO_2 clinopyroxene crystals in portions of the

Háleyjabunga analogue adjacent to magma-magma interfaces in the products of longer duration experiments.

Discussion

Diffusive controls over melt compositions. Although physical mingling is vital for homogenising mantle-derived chemical variability in primitive basalts, diffusion is ultimately required for all phases to attain equilibrium. In line with dynamic mixing experiments[30–32], our magma-magma reaction experiments suggest that chemically variable magmas must be mechanically thinned to filaments no more than a few mm wide for diffusive homogenisation to be achieved within the day-long timescales associated with mixing processes in basaltic plumbing systems[24,25]. Indeed, chemical variability in olivine-hosted melt inclusions from individual eruptions records the entrapment of variably mixed melts, suggesting that crystallisation and diffusive homogenisation occur over broadly similar timescales[8,15]. Our experiments also demonstrate that mixing can fractionate elements with different diffusivities (e.g., K_2O and TiO_2), potentially complicating records of mantle-derived chemical variability by processes described extensively in alkalic and evolved systems if not basaltic ones[30,34,57,58]. Moreover, diffusive fractionation has been implicated in creating high-field strength elements depletions in plagioclase-hosted melt inclusions from oceanic basalts[19,20], and it is at the µm-scale of melt inclusions that it will have its greatest effects. Thus, even transient modifications of melt compositions by diffusion could fundamentally skew our understanding of magmatic processes if they are captured by the melt inclusion archives upon which geological interpretations are often based[59].

Our estimated effective binary diffusion coefficients are not significantly affected by the presence of crystals at mass fractions of ~0.1–0.3. Error function fits through glass composition profiles reproduce compositions from crystal-rich portions of experimental products equally well as those from crystal-poor portions (Supplementary Fig. 2), and diffusivities estimated from these fits are consistent with those estimated from melt-only systems (Fig. 7)[35–38,46,47]. Furthermore, melt compositions close to initial magma-magma interfaces are not detectably affected by either plagioclase resorption or clinopyroxene re-crystallisation but are dominantly controlled by diffusion within the melt, with Fe loss to capsule materials imposing second-order controls in longer-duration

experiments. Our experiments thus suggest that the timescales over which basaltic magmas diffusively homogenise can be approximated by the re-equilibration of pure melts.

Mineral responses to diffusive changes in melt compositions. Primitive oceanic basalts inherit considerable chemical variability from the mantle[3–5], meaning that different batches of mantle-derived magma often have different bulk compositions at similar temperatures and degrees of magmatic evolution[8,9]. As a consequence, isothermal mixing between chemically variable magmas, as recorded by melt inclusion suites[8,15], is just as likely to occur as mixing between cool resident magmas and hot recharge magmas[17,18,24,27]. Thus, crystal cargoes will not only experience recharge-induced changes in temperature but also mixing-induced changes in carrier liquid chemistry under near-isothermal conditions. In turn, these changes in chemistry create disequilibrium conditions that drive isothermal crystal resorption and growth by, for example, constitutional undercooling[39,40].

Plagioclase crystals in our magma-magma reaction experiments responded to diffusion-induced changes in local melt compositions by resorbing completely within hours. While plagioclase crystals are typically euhedral to subhedral and often skeletal in experimental products derived from the Háleyjabunga analogue and unaffected by diffusion within the melt (Figs. 2a, 4a, 4b), those at the limits of plagioclase stability in the products of magma-magma reaction experiments are typically anhedral and cuspate (Fig. 9). Our magma-magma reaction experiments have thus captured plagioclase resorption in action. Specifically, plagioclase mass fractions decrease from far-field values of 0.11 to zero over distances of no more than ~200 μm. These short distances imply that plagioclase stability in our magma-magma reaction experiments was controlled by the kinetics of Al_2O_3 diffusion within the melt rather than plagioclase resorption at crystal-melt interfaces. In other words, the distribution of plagioclase crystals in our experimental products indicates that once local melt Al_2O_3 contents dropped below ~16 wt.%, plagioclase crystals up to 20 μm in length resorbed completely within a few hours. Encouragingly, this observation is consistent with published experiments demonstrating that anorthite in basaltic liquids can resorb at rates in excess of 10 μm/hour[38].

Olivine and clinopyroxene crystals also responded to diffusion-induced changes to local melt compositions, but in different ways from plagioclase crystals. The development of compositional

zoning in olivine crystals from longer-duration experiments suggests that they at least partly responded to isothermal changes in melt composition by diffusive re-equilibration in the solid state (Fig. 8a; Supplementary Fig. 1). Indeed, the partial re-equilibration of olivine crystals over lengthscales of ~10 μm within 24 hours is broadly consistent with a characteristic diffusion lengthscale (i.e. x, where $x \propto \sqrt{Dt}$)[45] of ~5 μm estimated using an Mg–Fe interdiffusion coefficient after Dohmen and Chakraborty[60], and provides independent validation of mixing timescales estimated from diffusion profiles in natural systems[25]. In contrast, clinopyroxene crystals seemingly responded to changes in local melt composition by resorption and re-crystallisation, as evidenced by steps in clinopyroxene TiO_2 content that progressively invade portions of experimental products derived from the Háleyjabunga analogue with increasing experimental duration (Fig. 8d). Importantly, these steps in clinopyroxene TiO_2 content are offset from magma-magma interfaces and coincide with diffusively controlled plagioclase resorption fronts, suggesting that they are not advective in origin. Moreover, clinopyroxene is denser than the melts we investigated (~3.3 versus ~2.7 g/cm^3), meaning that high-TiO_2 clinopyroxene could not have floated from the Stapafell analogue into the overlying Háleyjabunga analogue. The implications of our experimentally observed clinopyroxene re-crystallisation for natural systems remain unclear, however, partly because it is difficult to gauge how large natural crystals (>100 μm long) would respond from small experimentally produced crystals (≤10 μm long). It is nevertheless plausible that well-documented instances of isobaric clinopyroxene resorption in natural basalts record isobaric changes in magma chemistry as much as changes in magma temperature[12,61].

Magma mixing creates and modifies basaltic crystal cargoes. Mush disaggregation creates the crystal cargoes carried by many oceanic basalts[15,62,63], and the eruption of plagioclase glomerocrysts with quasi-cumulate textures is often interpreted as evidence of pre-eruptive crystal entrainment[21–23]. Although numerical modelling provides vital insights into the dynamics of crystal-rich magmas[64], the processes by which initially cohesive mushes disaggregate remain largely elusive. For example, primitive crystal cargoes are generally too refractory to be chemically excavated from cohesive mushes by the relatively evolved liquids that often carry them to the surface[15,22,62]. That is, assuming

evolution along a single liquid line of descent, the injection of liquids in equilibrium with relatively evolved plagioclase crystals ($X_{An} \leq 0.7$) would not unlock mushes of primitive plagioclase crystals ($X_{An} > 0.8$) but rather lock them up further by triggering the crystallisation of overgrowth rims. In nature, however, erupted crystal cargoes and carrier liquids are often derived from chemically distinct primary melt distributions that have evolved along different liquid lines of descent[22,65,66]. It is thus feasible that mush-derived crystals will have never been in equilibrium with melts parental to their eventual carrier liquids. A key consequence of this is that mush disaggregation may be triggered by differences in magma composition as well as by differences in magma temperature.

Chemical and isotopic disequilibria between basaltic melts and mush-derived high-X_{An} plagioclase crystals are well documented in oceanic basalts from ocean islands and mid-ocean ridges of all spreading rates[22,23,62,65,67,68], demonstrating that mixing between chemically variable primitive magmas is widespread in the oceanic realm[8,9]. Although pervasive evidence of mixing and disequilibrium does not in itself constrain the mechanisms by which mush disaggregation and crystal entrainment occur, it does highlight that the deep chemical variability required to trigger mush disaggregation by mixing-induced chemical disequilibrium and crystal resorption is globally present. Moreover, we speculate that variations in the H_2O content of arc magmas may have analogous effects to variations in the major element content of oceanic basalts, whereby the injection of H_2O-rich magmas may facilitate mush disaggregation by triggering plagioclase resorption[69].

Very few basalts erupted in oceanic settings are in equilibrium with high-X_{An} plagioclase at any stage of their evolution[15,62,70]. Instead, high-X_{An} plagioclase in oceanic settings probably crystallises from incompatible element-depleted primitive melts that are correspondingly enriched in refractory elements like CaO and Al_2O_3, and rarely survive crustal processing to erupt at the surface[7,70]. Indeed, these melts probably stall at depth where they form plagioclase-rich mushes and cumulates. Our magma-magma reaction experiments on chemically variable but naturalistic analogues of erupted Icelandic lavas suggest that injecting incompatible element-enriched and plagioclase-undersaturated magmas (like the Stapafell lava analogue) into high-X_{An} plagioclase-rich mushes (like the Háleyjabunga lava analogue but with a higher crystal fraction) could trigger mush disaggregation

without requiring hot recharge. This is important because primitive crystal cargoes in oceanic basalts typically show evidence of being entrained by cool and evolved magmas rather than hot and primitive ones[22,23,62]. We thus propose that the replacement of plagioclase-saturated mush liquids with plagioclase-undersaturated liquids can drive resorption within interstices and along grain boundaries that in turn unlocks mushes and facilitates crystal entrainment by ascending magmas (Fig. 10a).

While advection almost certainly drives magma mixing and mush melt replacement on the macro scale (>1 mm), diffusion is vital for changing melt compositions on the micro scale (<1 mm) of crystal-melt interactions that are ultimately responsible for determining crystal textures and controlling mush cohesion[31,32]. Although the lengthscales of plagioclase resorption we observe are short (~10 μm), partly reflecting the small size of plagioclase crystals in our experimental products with respect to natural samples (~10–20 versus >100 μm long), even modest amounts of resorption within interstices and along grain boundaries could trigger disaggregation[41]; large crystals do not need to resorb completely for mush cohesion to be lost, they merely need to become sufficiently detached to be entrained by their surrounding melts. That only modest amounts of resorption could enable mush disaggregation also bears on the relative volumes of different melts required to facilitate entrainment. Our lava analogues were reacted in approximately 50:50 proportions, meaning that melt Al_2O_3 contents would eventually reach sufficiently low levels throughout the experimental samples for all plagioclase crystals to resorb (i.e. below ~16.0 wt.%). Conversely, if the proportion of incompatible element-enriched lava analogue were below ~0.25 then plagioclase would be stable upon complete re-equilibration (i.e. melt Al_2O_3 contents would exceed ~16 wt.%), re-crystallising in regions where it had previously resorbed, albeit with a lower X_{An}. However, even transient resorption triggered by volumetrically minor injections of incompatible element-enriched magmas could permit the one-way process of disaggregation, with subsequent re-crystallisation feasibly contributing to the textural complexity of erupted crystals[21,23].

Regardless of their origins, crystal cargoes will be modified as physical mixing processes transfer them between liquids with different phase equilibria. The transfer of high-X_{An} plagioclase crystals between melts with different CaO and Al_2O_3 contents can thus result in either growth or

resorption depending on the direction of transfer. For example, our magma-magma reaction experiments at 1190 °C demonstrate how the diffusive equilibration of incompatible element-depleted and plagioclase-saturated magmas with incompatible element-enriched and plagioclase-undersaturated magmas can trigger isothermal plagioclase resorption in the former without plagioclase nucleation in the latter (Figs. 4, 8). At lower T conditions (~1170 °C[7]), however, isothermal Al_2O_3 diffusion may trigger plagioclase nucleation in initially plagioclase-free and incompatible element-enriched magmas rather than plagioclase resorption in initially plagioclase-bearing and incompatible element-depleted magmas because the former would be closer to plagioclase saturation than is the case in our experiments. In plagioclase-saturated but chemically variable systems at yet lower T conditions (≤1160 °C[7]), isothermal Al_2O_3, CaO and Na_2O diffusion could produce plagioclase crystals with X_{An} zonation. Comparable differences in behaviour could also arise by mixing magmas initially equilibrated at different pressures because plagioclase stability correlates with P[71].

Although decompression, primitive recharge and boundary layer effects doubtlessly contribute towards the textural complexity of plagioclase crystals in oceanic basalts[15,18,21,23], isothermal and isobaric changes in melt composition are also likely to be important. Indeed, mixing-induced changes in melt composition may drive the cycles of resorption and re-crystallisation implicated in the formation of plagioclase-hosted melt inclusions (Fig. 10b)[19,20]. Although correlated changes in temperature and melt composition will drive the largest diffusive changes in olivine X_{Fo} contents[24–26], X_{Fo} variations may also reflect isothermal variations in melt chemistry (Figs. 8a, 10c). Indeed, our experiments suggest that olivine crystals respond to changes in melt composition by diffusive re-equilibration rather than re-crystallisation. Conversely, our observations suggest that clinopyroxene crystals can respond to changes in melt composition, at least over short lengthscales, by resorption and re-crystallisation rather than diffusive re-equilibration (Fig. 10c). Some of the textural complexity observed in natural clinopyroxenes may thus result from mixing between chemically distinct primitive basalts[12,61].

Magma mixing creates and modifies basaltic crystal cargoes and can therefore alter magmatic plumbing system dynamics and erupted records of mantle-derived chemical variability. We therefore argue that crystal resorption in response to mixing-induced chemical disequilibrium represents a currently underappreciated yet potentially widespread mechanism for disaggregating crystal mushes that can also alter the viscosity, density and eruptibility of oceanic basalts through the entrainment of buoyant high-X_{An} plagioclase crystals in large volumes (sometimes >30 vol.%)[22,62]. Overall, isothermal mixing between chemically variable primitive magmas is likely to play an equally important role in generating the texturally and chemically complex crystal cargoes we observe at the surface as the more widely recognised process of primitive recharge.

Methods

Experimental methods. Synthesis experiments were performed in an internally heated pressure vessel (IHPV) at the Institut für Mineralogie of the Leibniz Universität Hannover, Germany. Experiments were performed at 300 MPa and 1190 °C to maximise differences in resulting phase assemblages and proportions according to published equilibrium phase relations[7]. Synthetic analogues of the incompatible-element depleted Háleyjabunga and incompatible element-enriched Stapafell lavas were prepared by Neave et al.[7] from reagent grade oxide and carbonate powders that were fused twice in Pt crucibles placed in a muffle furnace at 1600 °C. Each fusion was performed for 1 hour, after which the melt was quenched by pouring it onto a clean brass plate. Quenched glass chips were then powdered in an agate disc mill to ensure that starting materials were compositionally homogenous. About 300 mg of each powdered starting material was then loaded into $Au_{80}Pd_{20}$ capsules with external and internal diameters of 2.6 and 2.2 mm, respectively, and welded shut. Each capsule was ~25 mm long in order to maximise the volumes of synthetic magmas that could be produced in each IHPV experiment. Prior to being loaded with starting materials, capsules were pre-saturated with ~0.25 wt.% Fe to minimise Fe exchange between capsule materials and experimental samples following the procedures described by Husen et al.[71,72].

Prepared capsules were suspended from a Pt wire in the hot zone of the IHPV[73]. The IHPV was then pressurised to 300 MPa with Ar and heated to 1190 °C. Pressure was monitored with a strain gauge manometer and did not vary by more than 5 MPa; temperature was monitored with four unsheathed S-type thermocouples and did not vary by more than 5 °C. Experimental temperatures were approached by heating the furnace from room temperature to 10 °C below the target temperature at a rate of 50 °C/min; final heating from 1180 to 1190 °C was performed at a rate of 10 °C/min to avoid overshooting. For the magma synthesis experiments, thermal cycling (1190 ± 5 °C) was applied for the first 24 hours to promote the growth of large crystals[74]. Temperature was then kept constant for the last 48 hours. Experimental products were quenched after 72 hours by fusing the Pt wire on which the capsules were suspended. The capsules dropped into a cold zone at the bottom of the vessel cooled at a rate of ~150 °C/s, which was sufficient to avoid the formation of quench crystals.

All experiments were conducted under nominally dry conditions (no H_2O was added to the dried starting powders), which resulted in melt H_2O contents of ~0.7 wt.% following the reduction of Fe_2O_3 in the starting glasses to FeO and the inward diffusion of trace H_2 from the Ar pressure medium at high temperatures. These H_2O contents are consistent with the experiments having been run under broadly reducing conditions about one log unit above the fayalite-magnetite-quartz redox buffer (FMQ+1): melt H_2O contents of ~0.7 wt.% correspond to an a_{H_2O} of ~0.06[75], which is related to the $f_{O_2}^{sample}$ by the relationship $f_{O_2}^{sample} = f_{O_2}^{vessel} \cdot {a_{H_2O}}^2$, where $f_{O_2}^{vessel}$ was estimated as FMQ+3.3 based on the f_{O_2} of samples saturated in a pure H_2O fluid[76].

Magma-magma reaction experiments were performed under exactly the same conditions as synthesis experiments, and in the same IHPV. The products of each synthesis experiment were cut into four cylinders ~3.5 mm long, some of which were irregular because of the crimps used to seal capsule ends. The dimensions of these irregularities exceeded the dimensions of most diffusive features investigated here. The ends of the products of each synthesis experiment were retained to determine the phase assemblages and phase compositions present at the start of magma-magma reaction experiments. Magma cylinders from each synthesis experiment were then juxtaposed within new $Au_{20}Pd_{20}$ capsules with the same dimensions and approximate Fe contents as those used for synthesis experiments. Each capsule was then welded shut and magma-magma reaction experiments were performed in the same way as described for synthesis experiments. Capsules were oriented with cylinders synthesised from the relatively dense and FeO*-rich Stapafell lava analogue beneath those synthesised from the relatively light and FeO*-poor Háleyjabunga lava analogue to prevent intra-capsule convection[77]. Magma-magma reaction experiments were performed for durations of 1, 4, 24 and 96 hours in order to capture the time-dependent nature of kinetic processes. The products of magma-magma reaction experiments were cut longitudinally and mounted in resin alongside the reserved products of synthesis experiments for subsequent imaging and analysis.

Analytical methods. Experimental products were imaged by field emission gun scanning electron microscopy (FEG-SEM) on a JEOL JSM-7610F instrument at the Institut für Mineralogie of the Leibniz Universität Hannover, Germany. Backscatter electron images (BSE) were typically collected

using an accelerating voltage of 15 kV and a working distance of 15 mm. BSE maps of experimental products were acquired using Bruker's ESPRIT software.

The major and minor element compositions of experimental products were determined by electron probe microanalysis (EPMA) on a Cameca SX100 instrument at the Institut für Mineralogie of the Leibniz Universität Hannover, Germany. Silicon, Ti, Al, Cr, Fe, Mn, Mg, Ca, Na, K and P were measured in glasses with a beam size of 12 µm, an accelerating voltage of 15 kV and a current of 10 nA. Silicon, Ti, Al, Cr, Fe, Mn, Mg, Ca, Na and K were measured in minerals with a beam size of 1 µm, an accelerating voltage of 15 kV and a current of 15 nA. Elements were counted on peak for 20 s, with the exceptions of Si and Na that were counted on peak for 10 s to minimise detector drift and Na migration, respectively. Background counting times were half on-peak counting times. The following standards were used for calibration: wollastonite (Si and Ca), TiO_2 (Ti), jadeite (Al), Cr_2O_3 (Cr), Fe_2O_3 (Fe), Mn_3O_4 (Mn), MgO (Mg), albite (Na), orthoclase (K) and apatite (P). The following secondary standards were regularly analysed to correct for inter-session drift and to monitor accuracy and precision: VG-2 basaltic glass (NMNH 111240-52; using the preferred MgO content), Kakanui augite (NMNH 122142; using preferred values), San Carlos olivine (NMNH 111312-44) and Lake County plagioclase (NMNH 115900)[78]. Accuracy and precision were typically better than 2% and 2%, and 10% and 10% for major (>1 wt.%) and minor (<1 wt.%) elements, respectively. Typical analyses of standards are provided alongside analyses of experimental products in the Supplementary Data.

Glass H_2O contents were determined in the products of the synthesis experiments and 1- and 96-hour magma-magma reaction experiments by Fourier-transform infrared (FTIR) spectroscopy with a Bruker IFS88 instrument at the Institut für Mineralogie of the Leibniz Universität Hannover, Germany, following the methods described by Husen et al.[71]. Estimated glass H_2O contents are provided in the Supplementary Data with further information about experimental a_{H_2O}–f_{O_2} conditions.

Estimating effective binary diffusion coefficients. Effective binary diffusion coefficients (D) were estimated by fitting error functions to glass composition profiles through the products of magma-

magma reaction experiments to solve Fick's 2nd Law: $C(x,t) = C_1 + \frac{C_0 - C_1}{2}\left(1 - \mathrm{erf}\left(\frac{x}{2\sqrt{Dt}}\right)\right)$, where $C(x,t)$ is the concentration in wt.% of the diffusing element C at distance x in m after time t in s, and C_0 and C_1 are the initial concentrations of the diffusing element on either side of the couple[49]. Fitting was performed by minimising the χ^2 misfit associated with the following function: $y_{est} = a\,\mathrm{erf}\big(b(x+c)\big) + d$, where y_{est} is the predicted concentration of a given oxide in wt.% and a, b, c and d are fitting parameters. The χ^2 misfit was defined as follows: $\chi^2 = \sum_{x=0}^{n}\left(\frac{(y_{obs} - y_{est})^2}{2\sigma}\right)$, where y_{obs} is the observed concentration of a given oxide in wt.% at a distance of x, y_{est} is the predicted concentration of a given oxide in wt.% at a distance of x and σ is the uncertainty associated with analyses of a given oxide in wt.%. Minimisations were performed with the fminsearch() function implemented in the pracma package of R[79]. Element diffusivities in m^2/s were then calculated using the following relationship[45]: $D = \frac{((1/b)^2)}{4t}$, where b is the fitting parameter described above. Diffusion coefficients were only estimated for element-duration combinations for which composition profiles were clearly sigmoidal in form and had well-defined plateaux at each end. Thus, no diffusion coefficients were estimated from the products of the 96-hour experiment or for some elements (FeO*, CaO and Na_2O) in the products of 24-hour experiment. Uncertainties in diffusion coefficients were estimated by fitting composition profiles that had been repeatedly resampled according to the analytical uncertainties associated with each element.

Data availability

EMPA data and BSE maps are provided in the Supplementary Data.

509 **References**

510 1. Hofmann, A. W. & White, W. M. Mantle plumes from ancient oceanic crust. *Earth Planet.*
511 *Sci. Lett.* **57**, 421–436 (1982).

512 2. Gast, P. W. Trace element fractionation and the origin of tholeiitic and alkaline magma types.
513 *Geochim. Cosmochim. Acta* **32**, 1057–1086 (1968).

514 3. Hofmann, A. W. Mantle geochemistry: the message from oceanic volcanism. *Nature* **385**,
515 219–229 (1997).

516 4. Hirschmann, M. M. & Stolper, E. M. A possible role for garnet pyroxenite in the origin of the
517 'garnet signature' in MORB. *Contrib. to Mineral. Petrol.* **124**, 185–208 (1996).

518 5. Hauri, E. H. Major-element variability in the Hawaiian mantle plume. *Nature* **382**, 415–419
519 (1996).

520 6. Michael, P. J. & Chase, R. L. The influence of primary magma composition, H_2O and pressure
521 on mid-ocean ridge basalt differentiation. *Contrib. to Mineral. Petrol.* **96**, 245–263 (1987).

522 7. Neave, D. A., Namur, O., Shorttle, O. & Holtz, F. Magmatic evolution biases basaltic records
523 of mantle chemistry towards melts from recycled sources. *Earth Planet. Sci. Lett.* **520**, 199–
524 211 (2019).

525 8. Maclennan, J. Concurrent mixing and cooling of melts under Iceland. *J. Petrol.* **49**, 1931–1953
526 (2008).

527 9. Shorttle, O. Geochemical variability in MORB controlled by concurrent mixing and
528 crystallisation. *Earth Planet. Sci. Lett.* **424**, 1–14 (2015).

529 10. Rubin, K. H., Sinton, J. M., Maclennan, J. & Hellebrand, E. Magmatic filtering of mantle
530 compositions at mid-ocean-ridge volcanoes. *Nat. Geosci.* **2**, 321–328 (2009).

531 11. Saal, A. E., Hart, S. R., Shimizu, N., Hauri, E. H. & Layne, G. D. Pb isotopic variability in
532 melt inclusions from oceanic island basalts, Polynesia. *Science (80-.).* **282**, 1481–1484 (1998).

12. Winpenny, B. & Maclennan, J. A partial record of mixing of mantle melts preserved in Icelandic phenocrysts. *J. Petrol.* **52**, 1791–1812 (2011).

13. Maclennan, J. Lead isotope variability in olivine-hosted melt inclusions from Iceland. *Geochim. Cosmochim. Acta* **72**, 4159–4176 (2008).

14. Sobolev, A. V. & Shimizu, N. Ultra-depleted primary melt included in an olivine from the Mid-Atlantic Ridge. *Nature* **363**, 151–154 (1993).

15. Neave, D. A., Passmore, E., Maclennan, J., Fitton, J. G. & Thordarson, T. Crystal-melt relationships and the record of deep mixing and crystallization in the AD 1783 Laki eruption, Iceland. *J. Petrol.* **54**, 1661–1690 (2013).

16. Kuo, L. C. & Kirkpatrick, R. J. Pre-eruption history of phyric basalts from DSDP legs 45 and 46: Evidence from morphology and zoning patterns in plagioclase. *Contrib. to Mineral. Petrol.* **79**, 13–27 (1982).

17. Dungan, M. A. & Rhodes, J. M. Residual Glasses and Melt Inclusions in Basalts from DSDP Legs 45 and 46: Evidence for Magma Mixing. *Contrib. to Mineral. Petrol.* **67**, 417–431 (1978).

18. Rhodes, J. M., Dungan, M. A., Blanchard, D. P. & Long, P. E. Magma mixing at mid-ocean ridges: evidence from basalts drilled near 22°N on the Mid-Atlantic Ridge. *Tectonophysics* **55**, 35–61 (1979).

19. Michael, P. J., McDonough, W. F., Nielsen, R. L. & Cornell, W. C. Depleted melt inclusions in MORB plagioclase: Messages from the mantle or mirages from the magma chamber? *Chem. Geol.* **183**, 43–61 (2002).

20. Neave, D. A., Hartley, M. E., Maclennan, J., Edmonds, M. & Thordarson, T. Volatile and light lithophile elements in high-anorthite plagioclase-hosted melt inclusions from Iceland. *Geochim. Cosmochim. Acta* **205**, 100–118 (2017).

21. van Gerve, T. D., Neave, D. A., Almeev, R. R., Holtz, F. & Namur, O. Zoned crystal records

of transcrustal magma transport, storage and differentiation: insights from the Shatsky Rise oceanic plateau. *J. Petrol.* **61**, egaa080 (2020).

22. Neave, D. A., Maclennan, J., Hartley, M. E., Edmonds, M. & Thordarson, T. Crystal storage and transfer in basaltic systems: the Skuggafjöll eruption, Iceland. *J. Petrol.* **55**, 2311–2346 (2014).

23. Bennett, E. N., Lissenberg, C. J. & Cashman, K. V. The significance of plagioclase textures in mid-ocean ridge basalt (Gakkel Ridge, Arctic Ocean). *Contrib. to Mineral. Petrol.* **174**, 49 (2019).

24. Kahl, M., Chakraborty, S., Costa, F. & Pompilio, M. Dynamic plumbing system beneath volcanoes revealed by kinetic modeling, and the connection to monitoring data: An example from Mt. Etna. *Earth Planet. Sci. Lett.* **308**, 11–22 (2011).

25. Mutch, E. J. F., Maclennan, J., Shorttle, O., Edmonds, M. & Rudge, J. F. Rapid transcrustal magma movement under Iceland. *Nat. Geosci.* **12**, 569–574 (2019).

26. Costa, F., Shea, T. & Ubide, T. Diffusion chronometry and the timescales of magmatic processes. *Nat. Rev. Earth Environ.* **1**, 201–214 (2020).

27. Ubide, T. & Kamber, B. S. Volcanic crystals as time capsules of eruption history. *Nat. Commun.* **9**, 326 (2018).

28. Kouchi, A. & Sunagawa, I. Mixing basaltic and dacitic magmas by forced convection. *Nature* **304**, 527–528 (1983).

29. De Campos, C. P., Dingwell, D. B. & Fehr, K. T. Decoupled convection cells from mixing experiments with alkaline melts from Phlegrean Fields. *Chem. Geol.* **213**, 227–251 (2004).

30. Morgavi, D., Perugini, D., de Campos, C. P., Ertel-Ingrisch, W. & Dingwell, D. B. Time evolution of chemical exchanges during mixing of rhyolitic and basaltic melts. *Contrib. to Mineral. Petrol.* **166**, 615–638 (2013).

582 31. Rossi, S. *et al.* Exponential decay of concentration variance during magma mixing: Robustness
583 of a volcanic chronometer and implications for the homogenization of chemical
584 heterogeneities in magmatic systems. *Lithos* **286**–**287**, 396–407 (2017).

585 32. Laumonier, M., Scaillet, B., Arbaret, L. & Champallier, R. Experimental simulation of magma
586 mixing at high pressure. *Lithos* **196**–**197**, 281–300 (2014).

587 33. Kress, V. C. & Ghiorso, M. S. Multicomponent diffusion in MgO-Al_2O_3-SiO_2 and CaO-MgO-
588 Al_2O_3-SiO_2 melts. *Geochim. Cosmochim. Acta* **57**, 4453–4466 (1993).

589 34. González-Garcia, D. *et al.* Diffusive exchange of trace elements between alkaline melts:
590 Implications for element fractionation and timescale estimations during magma mixing.
591 *Geochim. Cosmochim. Acta* **233**, 95–114 (2018).

592 35. LaTourrette, T., Wasserburg, G. J. & Fahey, A. J. Self diffusion of Mg, Ca, Ba, Nd, Yb, Ti, Zr,
593 and U in haplobasaltic melt. *Geochim. Cosmochim. Acta* **60**, 1329–1340 (1996).

594 36. Chen, Y. & Zhang, Y. Olivine dissolution in basaltic melt. *Geochim. Cosmochim. Acta* **72**,
595 4756–4777 (2008).

596 37. Chen, Y. & Zhang, Y. Clinopyroxene dissolution in basaltic melt. *Geochim. Cosmochim. Acta*
597 **73**, 5730–5747 (2009).

598 38. Yu, Y., Zhang, Y., Chen, Y. & Xu, Z. Kinetics of anorthite dissolution in basaltic melt.
599 *Geochim. Cosmochim. Acta* **179**, 257–274 (2016).

600 39. Liang, Y. Kinetics of crystal-melt reaction in partially molten silicates: 1. Grain scale
601 processes. *Geochemistry, Geophys. Geosystems* **4**, 1045 (2003).

602 40. L'Heureux, I. Oscillatory zoning in crystal growth: A constitutional undercooling mechanism.
603 *Phys. Rev. E* **48**, 4460–4469 (1993).

604 41. Ruprecht, P., Simon, A. C. & Fiege, A. The Survival of Mafic Magmatic Enclaves and the
605 Timing of Magma Recharge. *Geophys. Res. Lett.* **47**, 1–9 (2020).

606 42. Shorttle, O. & Maclennan, J. Compositional trends of Icelandic basalts: Implications for short-
607 length scale lithological heterogeneity in mantle plumes. *Geochemistry, Geophys. Geosystems*
608 **12**, 1–32 (2011).

609 43. Neave, D. A. & Putirka, K. D. A new clinopyroxene-liquid barometer, and implications for
610 magma storage pressures under Icelandic rift zones. *Am. Mineral.* **102**, 777–794 (2017).

611 44. Barr, J. A. & Grove, T. L. AuPdFe ternary solution model and applications to understanding
612 the fO_2 of hydrous, high-pressure experiments. *Contrib. to Mineral. Petrol.* **160**, 631–643
613 (2010).

614 45. Zhang, Y. Diffusion in minerals and melts: theoretical background. *Rev. Mineral.*
615 *Geochemistry* **72**, 5–59 (2010).

616 46. Lundstrom, C. C. An experimental investigation of the diffusive infiltration of alkalis into
617 partially molten peridotite: Implications for mantle melting processes. *Geochemistry, Geophys.*
618 *Geosystems* **4**, 8614 (2003).

619 47. Lowry, R. K., Henderson, P. & Nolan, J. Tracer diffusion of some alkali, alkaline-earth and
620 transition element ions in a basaltic and an andesitic melt, and the implications concerning
621 melt structure. *Contrib. to Mineral. Petrol.* **80**, 254–261 (1982).

622 48. Zhang, Y., Ni, H. & Chen, Y. Diffusion data in silicate melts. *Rev. Mineral. Geochemistry* **72**,
623 311–408 (2010).

624 49. Crank, J. *The Mathematics of Diffusion*. (Clarendon Press, 1975).

625 50. Giordano, D., Russell, J. K. & Dingwell, D. B. Viscosity of magmatic liquids: A model. *Earth*
626 *Planet. Sci. Lett.* **271**, 123–134 (2008).

627 51. Glasstone, S., Laider, K. J. & Eyring, H. *The Theory of Rate Processes*. (McGraw-Hill, 1941).

628 52. Dingwell, D. B. Effects of structural relaxation on cationic tracer diffusion in silicate melts.
629 *Chem. Geol.* **82**, 209–216 (1990).

630 53. Mungall, J. E. Empirical models relating viscosity and tracer diffusion in magmatic silicate
631 melts. *Geochim. Cosmochim. Acta* **66**, 125–143 (2002).

632 54. Kirkpatrick, R. J. Crystal growth from the melt: a review. *Am. Mineral.* **60**, 798–814 (1975).

633 55. Neave, D. A. *et al.* Clinopyroxene–liquid equilibria and geothermobarometry in natural and
634 experimental tholeiites: the 2014–2015 Holuhraun eruption, Iceland. *J. Petrol.* **60**, 1653–1680
635 (2019).

636 56. Cherniak, D. J. & Liang, Y. Ti diffusion in natural pyroxene. *Geochim. Cosmochim. Acta* **98**,
637 31–47 (2012).

638 57. Perugini, D., De Campos, C. P., Dingwell, D. B., Petrelli, M. & Poli, G. Trace element
639 mobility during magma mixing: Preliminary experimental results. *Chem. Geol.* **256**, 146–157
640 (2008).

641 58. Laeger, K. *et al.* High-resolution geochemistry of volcanic ash highlights complex magma
642 dynamics during the Eyjafjallajökull 2010 eruption. *Am. Mineral.* **102**, 1173–1186 (2017).

643 59. Kent, A. J. R. Melt inclusions in basaltic and related volcanic rocks. *Rev. Mineral.*
644 *Geochemistry* **69**, 273–331 (2008).

645 60. Dohmen, R. & Chakraborty, S. Fe-Mg diffusion in olivine II: Point defect chemistry, change
646 of diffusion mechanisms and a model for calculation of diffusion coefficients in natural
647 olivine. *Phys. Chem. Miner.* **34**, 409–430 (2007).

648 61. Caricchi, L. *et al.* A Data Driven Approach to Investigate the Chemical Variability of
649 Clinopyroxenes From the 2014–2015 Holuhraun–Bárdarbunga Eruption (Iceland). *Front.*
650 *Earth Sci.* **8**, 1–15 (2020).

651 62. Lange, A. E., Nielsen, R. L., Tepley, F. J. & Kent, A. J. R. The petrogenesis of plagioclase-
652 phyric basalts at mid-ocean ridges. *Geochemistry, Geophys. Geosystems* **14**, 3282–3296
653 (2013).

63. Holness, M. B. *et al.* Textures in partially solidified crystalline nodules: A window into the pore structure of slowly cooled mafic intrusions. *J. Petrol.* **48**, 1243–1264 (2007).

64. Bergantz, G. W., Schleicher, J. M. & Burgisser, A. Open-system dynamics and mixing in magma mushes. *Nat. Geosci.* **8**, 793–796 (2015).

65. Halldórsson, S. A. *et al.* Isotopic-heterogeneity of the Thjorsa lava-Implications for mantle sources and crustal processes within the Eastern Rift Zone, Iceland. *Chem. Geol.* **255**, 305–316 (2008).

66. Lange, A. E., Nielsen, R. L., Tepley, F. J. & Kent, A. J. R. Diverse Sr isotope signatures preserved in mid-oceanic-ridge basalt plagioclase. *Geology* **41**, 279–282 (2013).

67. Ridley, I. W., Perfit, M. R., Smith, M. C. & Fornari, D. J. Magmatic processes in developing oceanic crust revealed in a cumulate xenolith collected at the East Pacific Rise, 9°50'N. *Geochemistry, Geophys. Geosystems* **7**, Q12O04 (2006).

68. Costa, F., Coogan, L. A. & Chakraborty, S. The time scales of magma mixing and mingling involving primitive melts and melt-mush interaction at mid-ocean ridges. *Contrib. to Mineral. Petrol.* **159**, 371–387 (2010).

69. Sisson, T. W. & Grove, T. L. Experimental investigations of the role of H_2O in calc-alkaline differentiation and subduction zone magmatism. *Contrib. to Mineral. Petrol.* **113**, 143–166 (1993).

70. Grove, T. L., Kinzler, R. J. & Bryan, W. B. Fractionation of Mid-Ocean Ridge Basalt (MORB). in *Mantle Flow and Melt Generation at Mid-Ocean Ridges, Geophysical Monograph 71* 281–310 (American Geophysical Union, 1992).

71. Husen, A., Almeev, R. R. & Holtz, F. The Effect of H_2O and Pressure on Multiple Saturation and Liquid Lines of Descent in Basalt from the Shatsky Rise. *J. Petrol.* **57**, 309–344 (2016).

72. Gaetani, G. A. & Grove, T. L. The influence of water on melting of mantle peridotite. *Contrib. to Mineral. Petrol.* **131**, 323–346 (1998).

679 73. Berndt, J. *et al.* A combined rapid-quench and H_2-membrane setup for internally heated
680 pressure vessels: Description and application for water solubility in basaltic melts. *Am.*
681 *Mineral.* **87**, 1717–1726 (2002).

682 74. Erdmann, M. & Koepke, J. Experimental temperature cycling as a powerful tool to enlarge
683 melt pools and crystals at magma storage conditions. *Am. Mineral.* **101**, 960–969 (2016).

684 75. Aranovich, L. Y. & Newton, R. C. Experimental determination of CO_2-H_2O activity-
685 composition relations at 600-1000 °C and 6-14 kbar by reversed decarbonation and
686 dehydration reactions. *Am. Mineral.* **84**, 1319–1332 (1999).

687 76. Botcharnikov, R. E., Koepke, J., Holtz, F., McCammon, C. & Wilke, M. The effect of water
688 activity on the oxidation and structural state of Fe in a ferro-basaltic melt. *Geochim.*
689 *Cosmochim. Acta* **69**, 5071–5085 (2005).

690 77. Zhang, Y., Walker, D. & Lesher, C. E. Diffusive crystal dissolution. *Contrib. to Mineral.*
691 *Petrol.* **102**, 492–513 (1989).

692 78. Jarosewich, E., Nelen, J. A. & Norberg, J. A. Reference samples for electron microprobe
693 analysis. *Geostand. Newsl.* **4**, 43–47 (1980).

694 79. R Development Core Team. R: A Language and Environment for Statistical Computing. *R*
695 *Found. Stat. Comput.* (2016).

696 **Acknowledgements**

697 We thank Ulrich Kroll and Stefan Linsler for their help with maintaining IHPV equipment, and Renat
698 Almeev and Chao Zhang for their help with EPMA. We also thank Mickael Laumonier, Tom Shea
699 and one anonymous reviewer for their detailed and highly constructive comments. This work and
700 DAN were supported by the German Research Foundation (DFG; NE2097/1-1). DAN was also
701 supported Presidential Fellowship from the University of Manchester and a NERC Independent
702 Research Fellowship (NE/T011106/1).

703 **Author contributions**

DAN designed the project and secured funding. PB performed the experiments and EPMA analyses under the supervision of DAN and FH. HB performed the FTIR analyses. All authors contributed to data interpretation. DAN wrote the manuscript with contributions from PB, HB and FH.

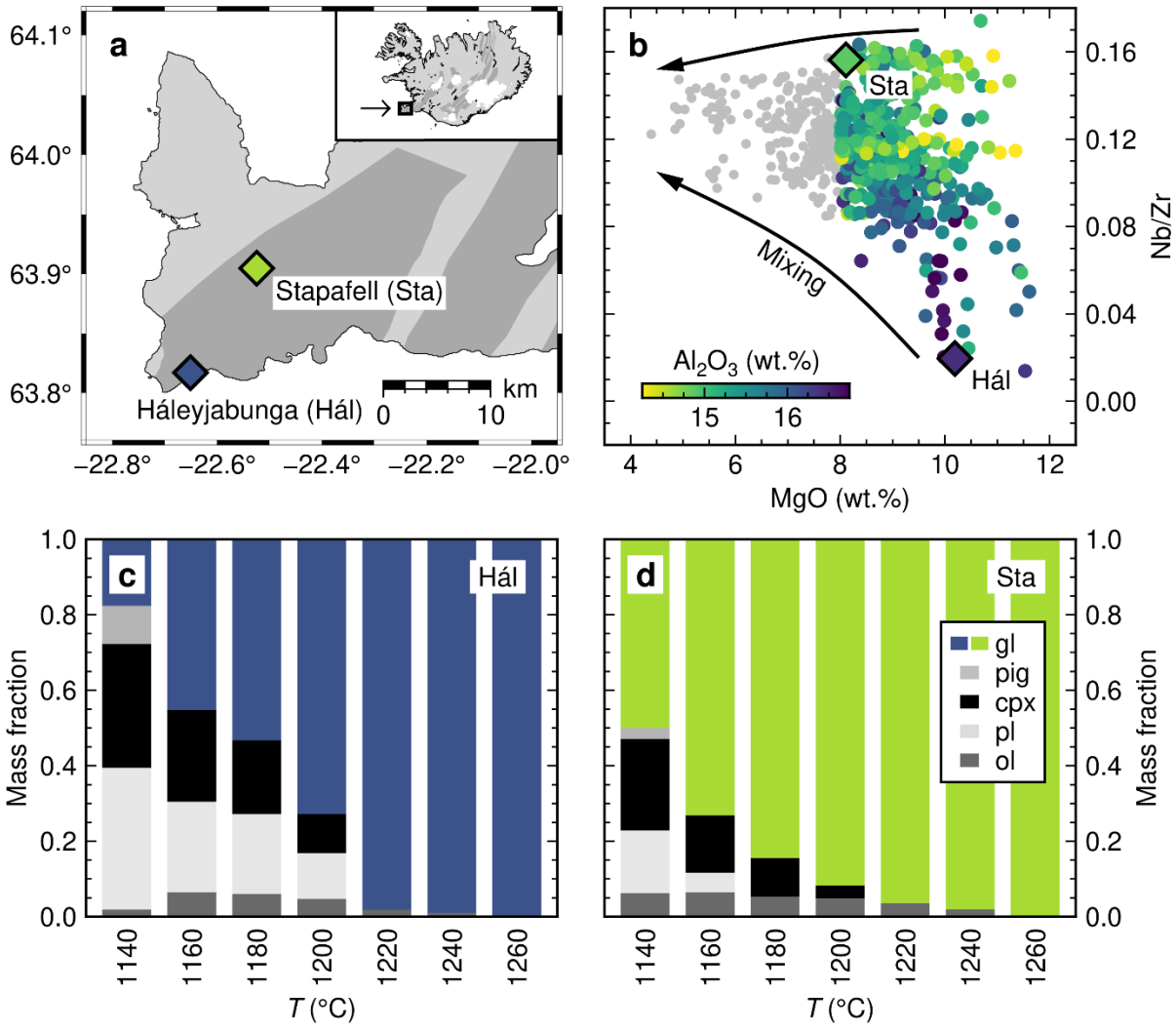

Fig. 1 Mantle-derived chemical variability in Icelandic basalts and its effects on the phase equilibria of primitive magmas. a Locations of the incompatible element-depleted Háleyjabunga (Hál) and incompatible element-enriched Stapafell (Sta) lavas on the Reykjanes Peninsula of southwest Iceland. Volcanic systems are highlighted in dark grey. **b** Summary of major and trace element variability in lavas from southwest Iceland[42]. MgO reflects the degree of magmatic evolution and Nb/Zr the degree of mantle-derived incompatible element enrichment. At any given MgO content, incompatible element-enriched lavas like those from Stapafell have lower Al_2O_3 contents than incompatible-element depleted lavas like those from Háleyjabunga. Arrows illustrate the reduction in chemical variability that results from concurrent mixing and crystallisation during magmatic evolution[8,9]. **c, d** Phase equilibria of Háleyjabunga (**c**) and Stapafell (**d**) lava analogues derived from crystallisation experiments at 300 MPa[7]. Equilibrium phase assemblages and proportions are related

719 to the degree of incompatible element enrichment: plagioclase crystallises at higher temperatures and
720 in greater amounts from incompatible element-depleted magmas that are correspondingly enriched in
721 refractory elements like CaO and Al_2O_3. Phases are labelled as follows: gl, glass; pig, pigeonite; cpx,
722 clinopyroxene; pl, plagioclase; and ol, olivine.

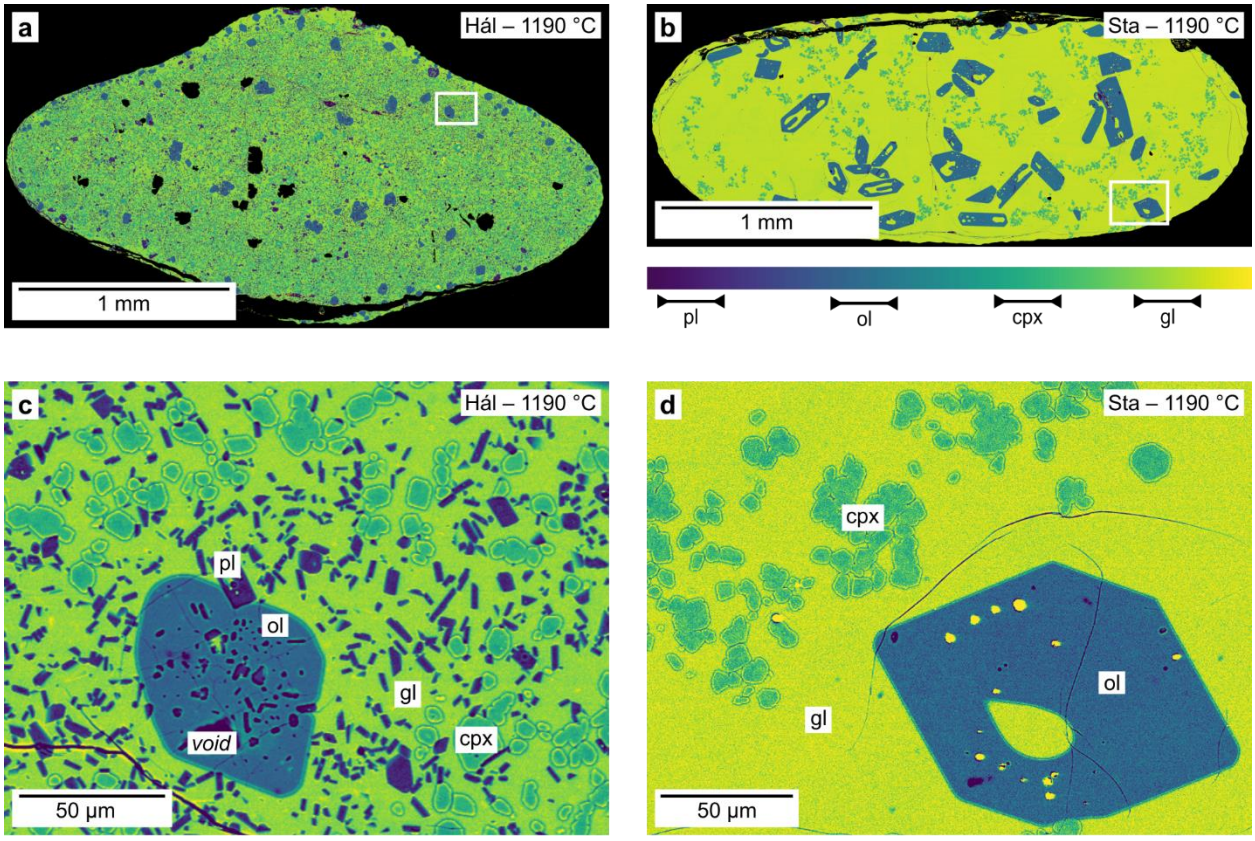

723

724 **Fig. 2 False-colour backscattered electron (BSE) images of the products of synthesis**
725 **experiments.** Synthesis experiments on Háleyjabunga (Hál) and Stapafell (Sta) lava analogues were
726 both performed at 300 MPa and 1190 °C. These conditions were chosen to maximise differences in
727 equilibrium phase equilibria[7]. **a** Products of the synthesis experiment on the incompatible element-
728 depleted Háleyjabunga lava analogue contain relatively modest amounts of glass [gl, yellow-green;
729 melt mass fraction (F) ~ 0.72]. Black areas within the products are voids and cracks generated during
730 polishing. **b** Products of the synthesis experiment on the incompatible element-enriched Stapafell lava
731 analogue contain relatively large amounts of glass (gl; F ~ 0.90). **c, d** High-resolution images of (**a**)
732 and (**b**) showing crystals of olivine (ol, blue), clinopyroxene (cpx, blue-green) and plagioclase (pl,
733 purple) in the products of the experiment on the Háleyjabunga analogue (**c**), and olivine and
734 clinopyroxene crystals in the products of the experiments of the Stapafell analogue (**d**).

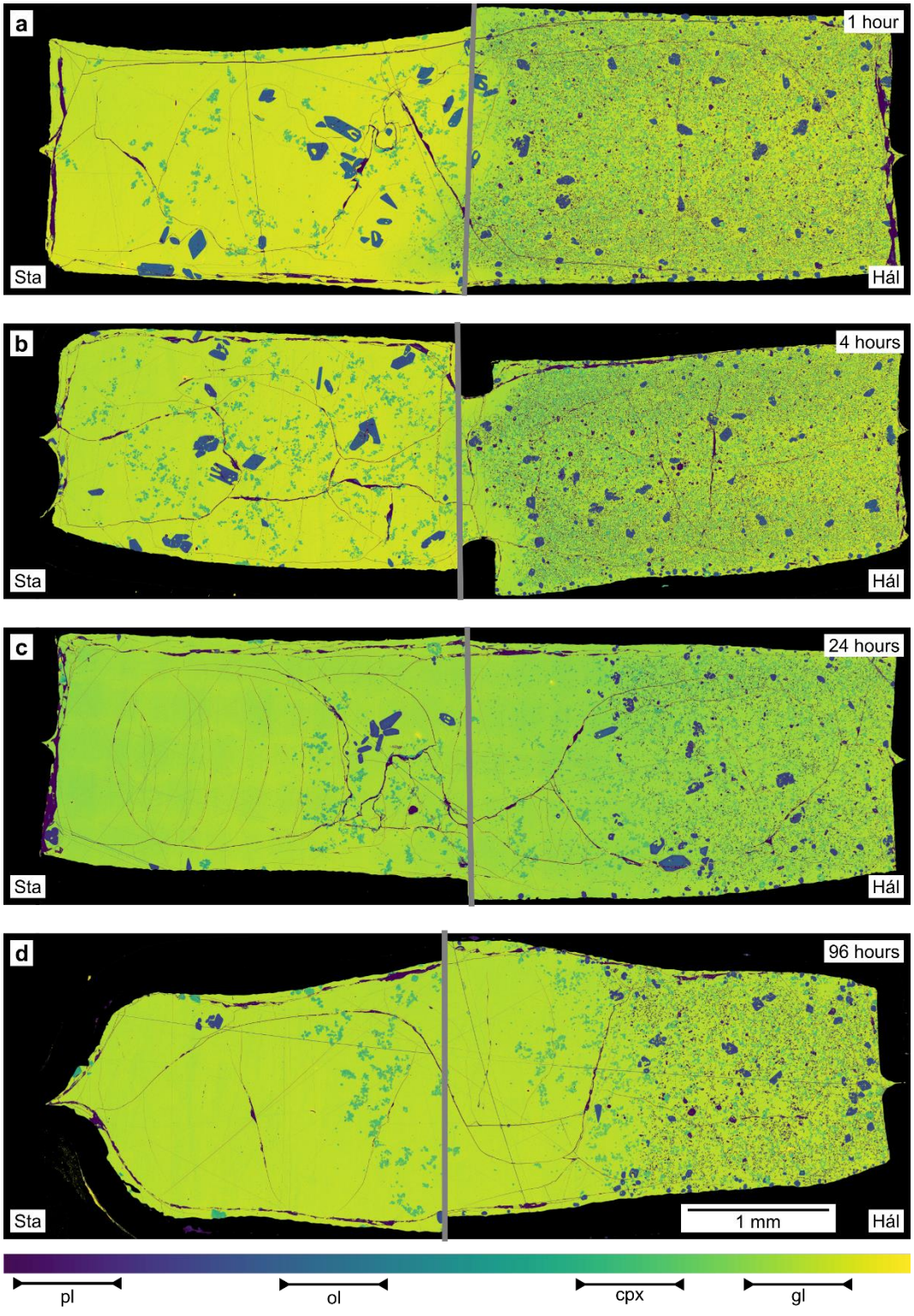

735

736 **Fig. 3 False-colour backscattered electron (BSE) maps of the products of magma-magma**

737 **reaction experiments.** Magma-magma reaction experiments were performed by juxtaposing

738 quenched magma cylinders from synthesis experiments on both Háleyjabunga (Hál) and Stapafell

739 (Sta) lava analogues within new capsules. These new capsules were then subjected to exactly the

same conditions used during synthesis experiments (300 MPa and 1190 °C). **a–d** BSE maps show the products of experiments run for 1 hour (**a**), 4 hours (**b**), 24 hours (**c**) and 96 hours (**d**). Magma cylinders synthesised from the incompatible element-depleted Háleyjabunga lava analogue are on the right, and magma cylinders synthesised from the incompatible element-enriched Stapafell lava analogue are on the left. Grey lines show the positions of original interfaces between juxtaposed magma cylinders. Plagioclase (pl) is the lowest BSE intensity phase (purple, only towards the right), followed, in order of increasing intensity, by olivine (ol, blue), clinopyroxene (cpx, blue-green) and glass (gl, green to yellow). Occasional bright flecks are small fragments of capsule material detached during sample preparation and are of no geological significance.

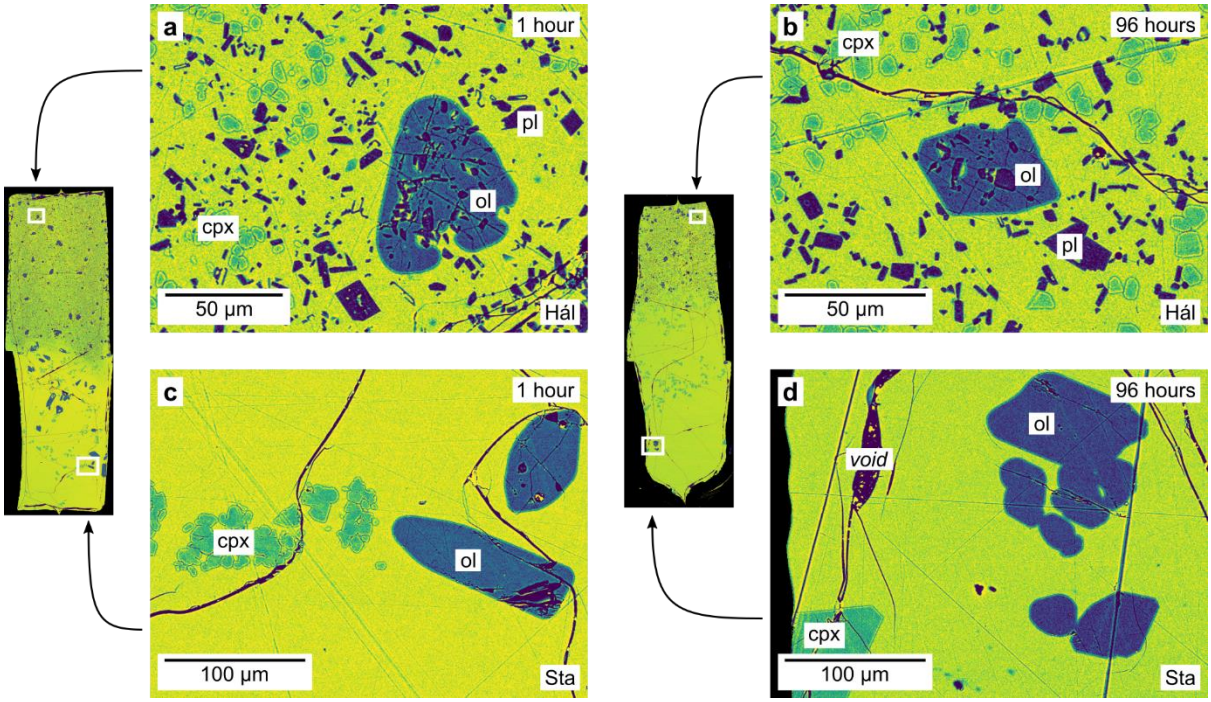

Fig. 4 False-colour backscattered electron (BSE) images of the products of 1- and 96-hour magma-magma reaction experiments. a, b Neither the far-field texture nor abundance of crystals change appreciably in portions of the experimental products derived from the Háleyjabunga lava analogue far from original magma-magma interfaces as experimental duration increases from 1 hour (**a**) to 96 hours (**b**). There is no clear evidence of Ostwald ripening in these portions of our experimental products. **c, d** Although the far-field abundance of crystals appears to decrease in portions of experimental products derived from the Stapafell lava analogue far from original magma-magma interfaces as experimental duration increases from 1 hour (**c**) to 96 hours (**d**), crystal textures remain mostly the same. Specifically, while olivine crystals have similar sizes and textures after 1 and 96 hours, clinopyroxene crystals may have decreased in number and increased in size by Ostwald ripening (i.e. coarsening).

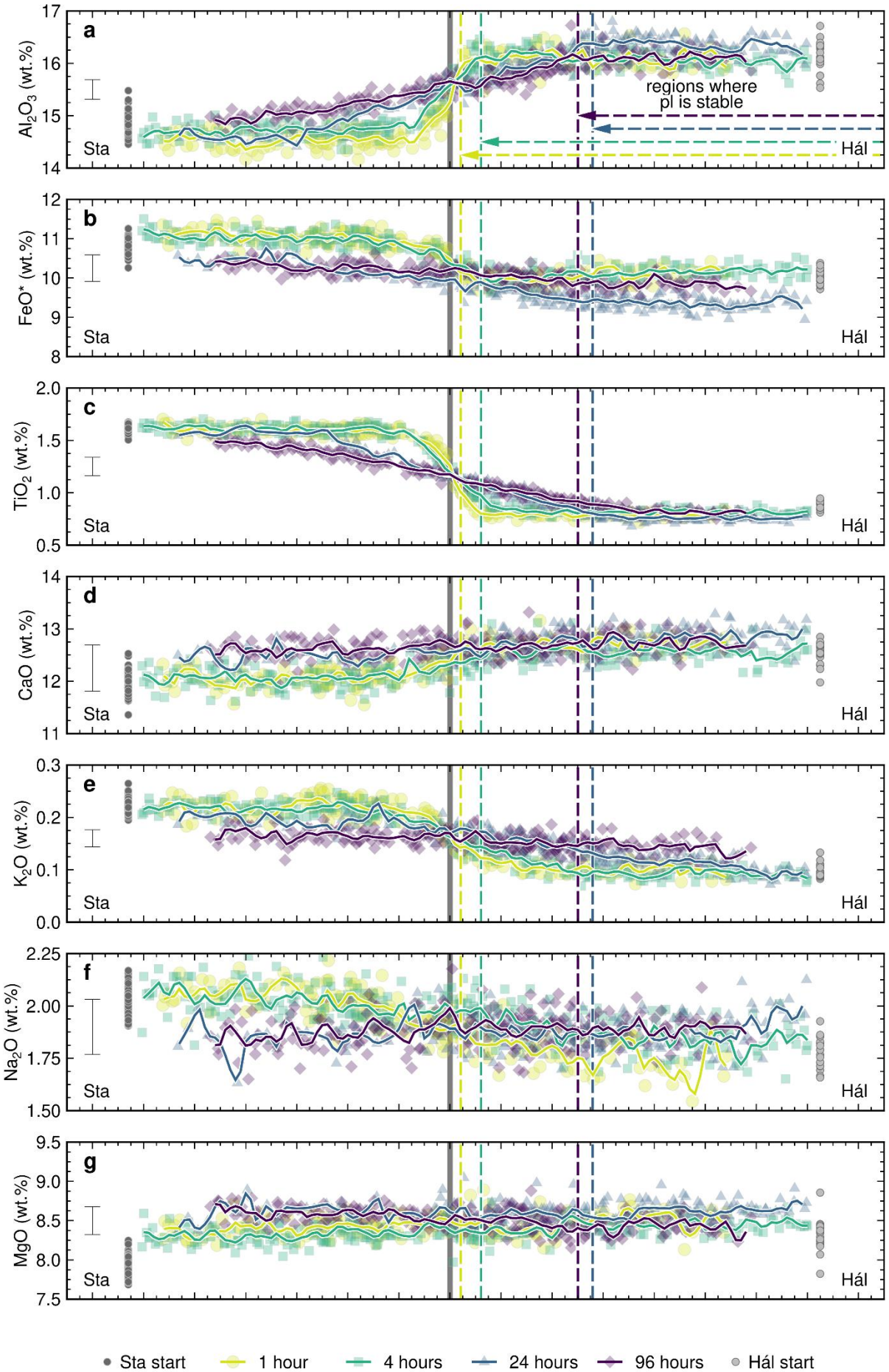
a
b
c
d
e
f
g
Al2O3 (wt.%)
FeO* (wt.%)
TiO2 (wt.%)
CaO (wt.%)
K2O (wt.%)
Na2O (wt.%)
MgO (wt.%)
Sta
Hál
regions where
pl is stable
Sta start
1 hour
4 hours
24 hours
96 hours
Hál start

Fig. 5 Glass composition profiles through the products of magma-magma reaction experiments. Glass composition profiles are centred on original magma-magma interfaces, which are indicated by vertical grey lines. Analyses from the products of experiments with different durations are shown with different colours and symbols. Solid lines show moving averages calculated by applying a Gaussian filter with a 0.25 mm bandwidth to raw analyses. Regions of the experimental products where plagioclase (pl) is stable are shown with dashed vertical lines and horizontal arrows. Compositions of glasses in the products of synthesis experiments are shown with grey symbols. Characteristic 2σ analytical uncertainties are shown. **a–f** Glass composition profiles in approximate order of increasing element diffusivity[48]: Al_2O_3 (**a**), FeO* (**b**), TiO_2 (**c**), CaO (**d**), K_2O (**e**) and Na_2O (**f**). **a–c** Relatively slow-diffusing elements typically show composition profiles with sigmoidal shapes for all experimental durations. Sigmoidal profiles are especially clear in the cases of Al_2O_3 (**a**) and TiO_2 (**c**) but obfuscated by Fe loss for experimental durations ≥24 hours in the case of FeO* (**b**). **d–f** Relatively fast-diffusing elements only show composition profiles with sigmoidal shapes for short experimental durations. This is emphasised most by Na_2O (**f**) for which initial variability is erased within 24 hours. (**g**) MgO shows little variability along compositional profiles beyond analytical uncertainty; small offsets between the products of synthesis and reaction experiments indicate that the former experienced slightly lower temperatures than the latter.

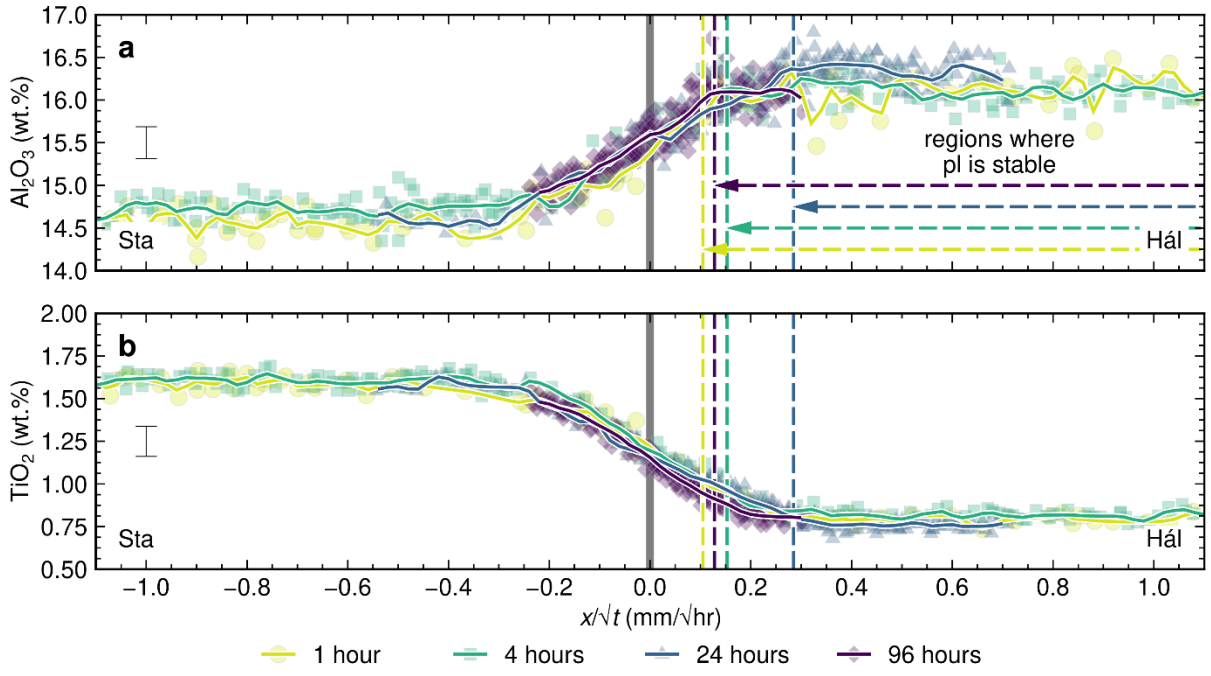

780

781 **Fig. 6 Time-normalised glass composition profiles through the products of magma-magma**
782 **reaction experiments.** Normalising glass composition profiles by the square root of experimental
783 duration eliminates the effects of time on the evolution of diffusively controlled profiles, which thus
784 collapse onto single curves for each element[34,48]. Symbols are the same as in Fig. 5. **a, b** Closely
785 overlapping time-normalised glass compositions profiles for Al_2O_3 (**a**) and TiO_2 (**b**) confirm that
786 chemical variability in the products of magma-magma reaction experiments was dominantly
787 controlled by diffusion within experimental melts. Equivalent profiles are shown for all elements in
788 Supplementary Fig. 3.

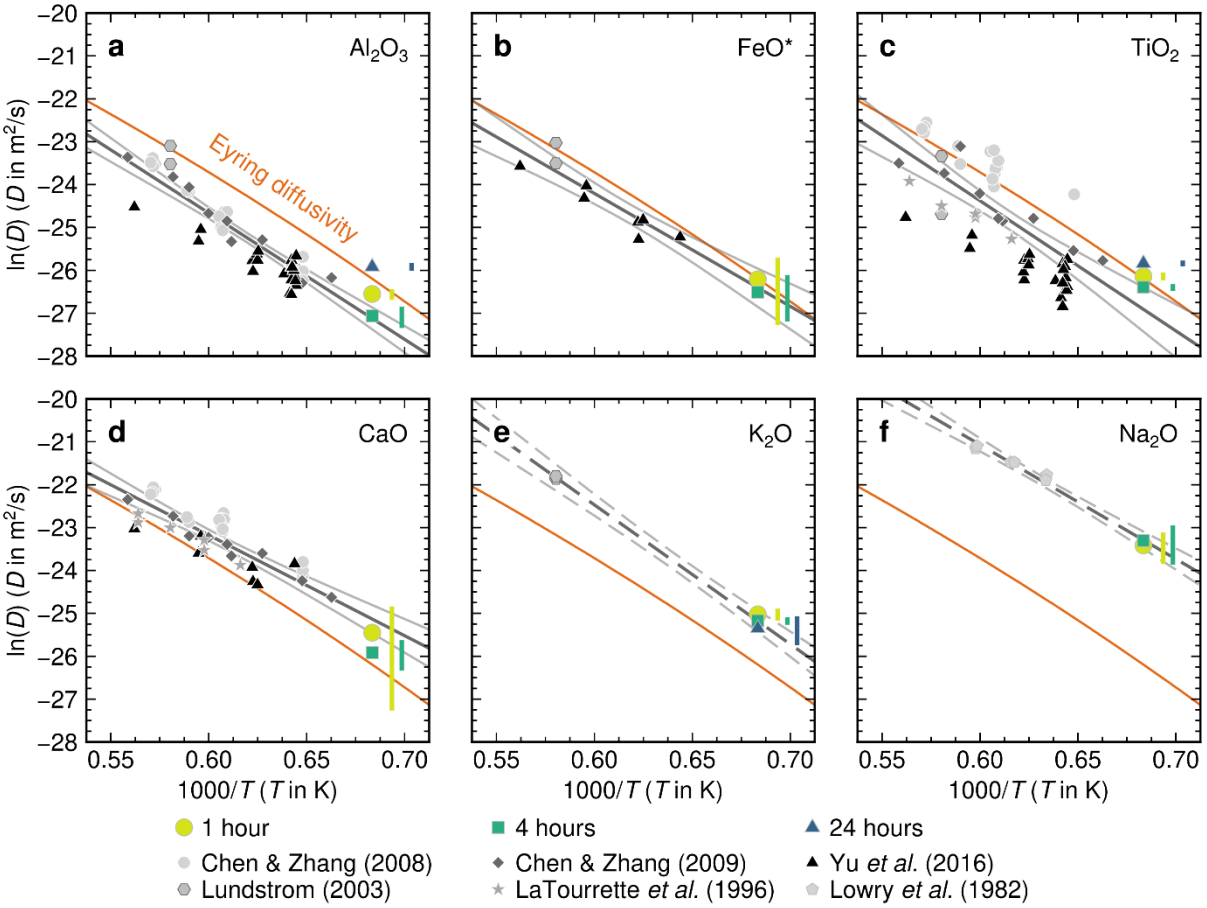

Fig. 7 Element diffusivities in basaltic melts. Effective binary diffusion coefficients (*D*) were estimated by fitting error functions to glass composition profiles to solve Fick's 2nd Law, and are summarised in 1000/*T* versus ln(*D*) space alongside published diffusivities from experiments on basaltic systems[35–38,46,47]. Diffusion coefficients estimated from our experiments are only presented for element-duration combinations for which composition profiles were clearly sigmoidal in form. Temperature- and viscosity-dependent Eyring diffusivities calculated with a characteristic diffusive jump length of 0.4 nm are shown as orange lines[34,51]. Grey lines show regressions with 95% confidence intervals through global datasets. Dashed lines show tentative regressions for elements with sparse diffusion data. Vertical coloured bars show 1σ uncertainties in diffusion coefficients offset for clarity. **a** Estimated Al_2O_3 diffusivities are broadly consistent with Eyring diffusivities and slightly faster than from published diffusivities[36–38,46]. **b** Estimated FeO* diffusivities are similar to Eyring diffusivities and consistent with published diffusivities[38,46] **c** Estimated TiO_2 diffusivities are similar to Eyring diffusivities and consistent with many published diffusivities, though published values span up

803 to three ln units at any given temeprature[35–38,46]. **d** Estimated CaO diffusivities are slightly faster than
804 Eyring diffusivities but appear slightly slower than published diffusivities[35–38]. **e** Estimated K_2O
805 diffusivities are a ln unit faster than Eyring diffusivities but define a plausible array in 1000/*T* versus
806 ln(*D*) space with the limited number of published diffusivities available[46]. **f** Estimated Na_2O
807 diffusivities are three ln units faster than Eyring diffusivities. They are also coherent with some
808 published diffusivities[47], but not others[37].

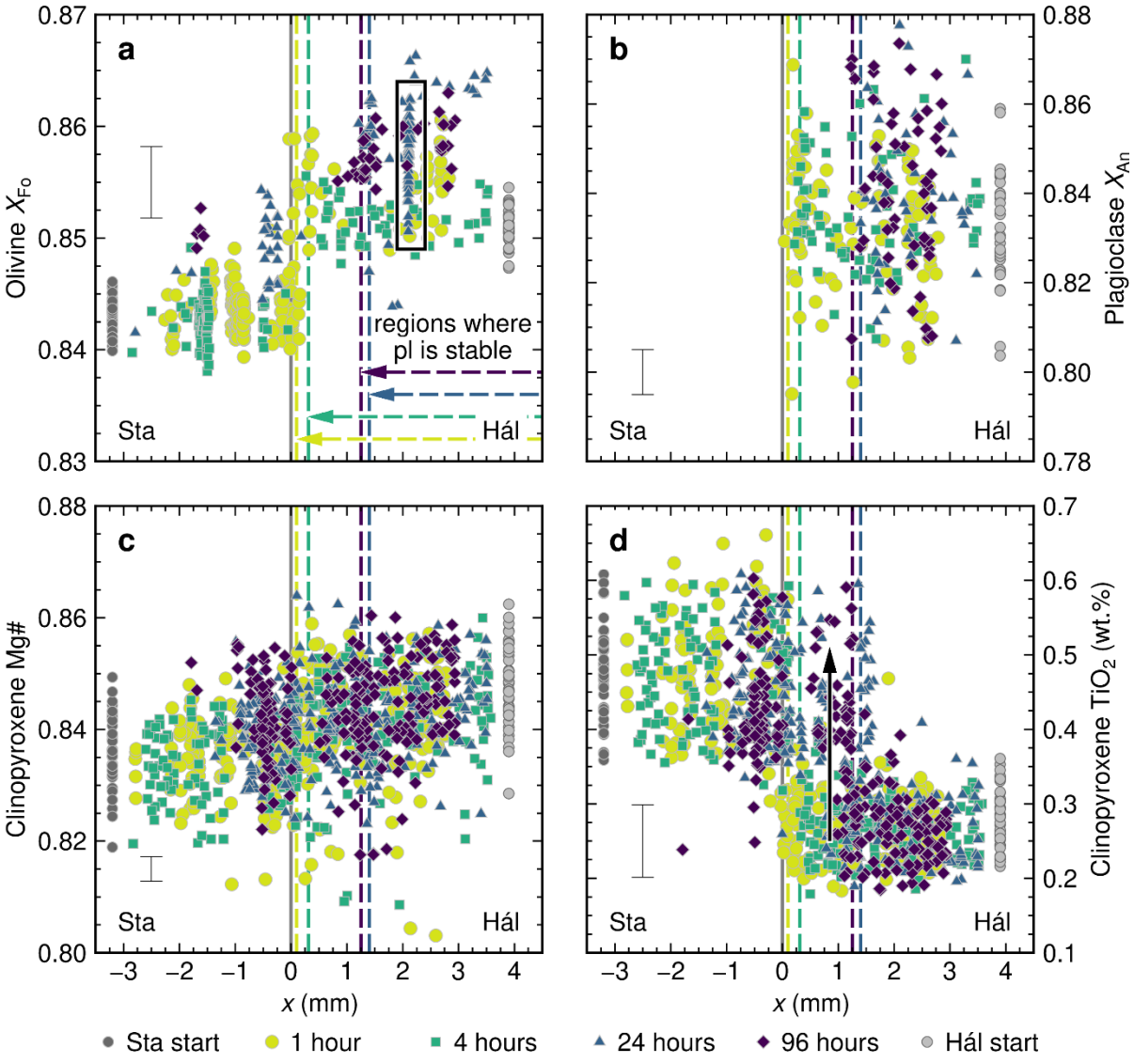

Fig. 8 Mineral compositions in the products of magma-magma reaction experiments. The positions of interfaces between juxtaposed magma cylinders are shown as vertical grey lines. Regions of the experimental products within which plagioclase (pl) is stable are shown with dashed vertical lines and horizontal arrows. Mineral compositions in the products of synthesis experiments are shown with grey symbols. Characteristic 2σ analytical uncertainties are shown. **a** Distribution of olivine compositions across the products of magma-magma reaction experiments summarised in terms of olivine forsterite content [X_{Fo}, where X_{Fo} = Mg/(Mg+Fe) on molar a basis]. Steps in X_{Fo} across interfaces between magma analogues reflect the higher FeO* content of the incompatible element-enriched Stapafell lava analogue with respect to the incompatible element-depleted Háleyjabunga analogue. Iron loss and diffusive re-equilibration of melt FeO* contents appear to have triggered the

diffusive re-equilibration of X_{Fo} in some crystals (one example is outlined in black box; Supplementary Fig. 1). **b** Distribution of plagioclase compositions across the products of magma-magma reaction experiments summarised in terms of plagioclase anorthite content [X_{An}, where X_{An} = Ca/(Ca+Na+K) on a molar basis]. The region where plagioclase is stabile contracts significantly as a function of increasing experimental duration as a result of plagioclase resorption in response to diffusively driven changes in melt compositions. Although X_{An} is somewhat variable, potentially as a consequence of rapid crystal growth during synthesis experiments[54], it does not vary systematically with position or experimental duration. **c** Distribution of clinopyroxene compositions across the products of magma-magma reaction experiments summarised in terms of clinopyroxene Mg-number [$Mg\#_{cpx}$, where $Mg\#_{cpx}$ = Mg/(Mg+Fe) on a molar basis]. While much variability in $Mg\#_{cpx}$ reflects the development of clinopyroxene sector zoning[55], mean $Mg\#_{cpx}$ contents are slightly higher in the FeO*-poor Háleyjabunga analogue than the FeO*-rich Stapafell analogue. **d** Distribution of clinopyroxene compositions across the products of magma-magma reaction experiments summarised in terms of clinopyroxene TiO_2 contents. Clinopyroxene crystals from the incompatible element-enriched Stapafell analogue are richer in TiO_2 than those from the incompatible element-depleted Háleyjabunga analogue. Moreover, clinopyroxene crystals within regions of plagioclase resorption have high TiO_2 contents, suggesting that plagioclase resorption is spatially correlated with the resorption and re-crystallisation of clinopyroxene, as indicated by the black arrow.

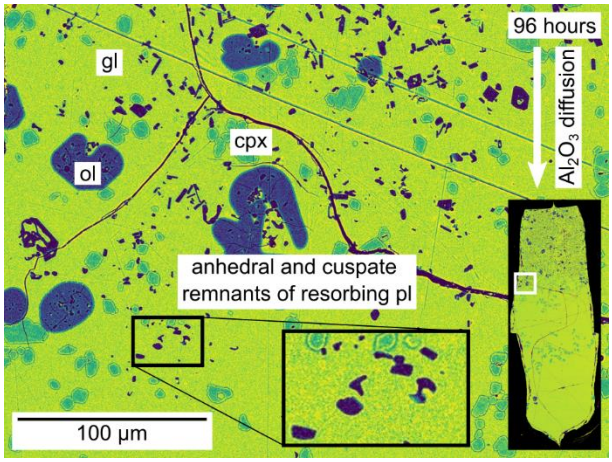

838

839 **Fig. 9 False-colour backscattered electron (BSE) image showing plagioclase resorption in the**
840 **products of the 96-hours magma-magma reaction experiment.** Many plagioclase (pl) crystals
841 close to plagioclase resorption fronts show resorbed textures, and the last remnants of resorbing
842 plagioclase crystals are especially anhedral and cuspate (see inset). Some olivine (ol) crystals close to
843 plagioclase resorption fronts are anhedral and embayed, whereas clinopyroxene (cpx) crystals retain
844 euhedral to subhedral textures.

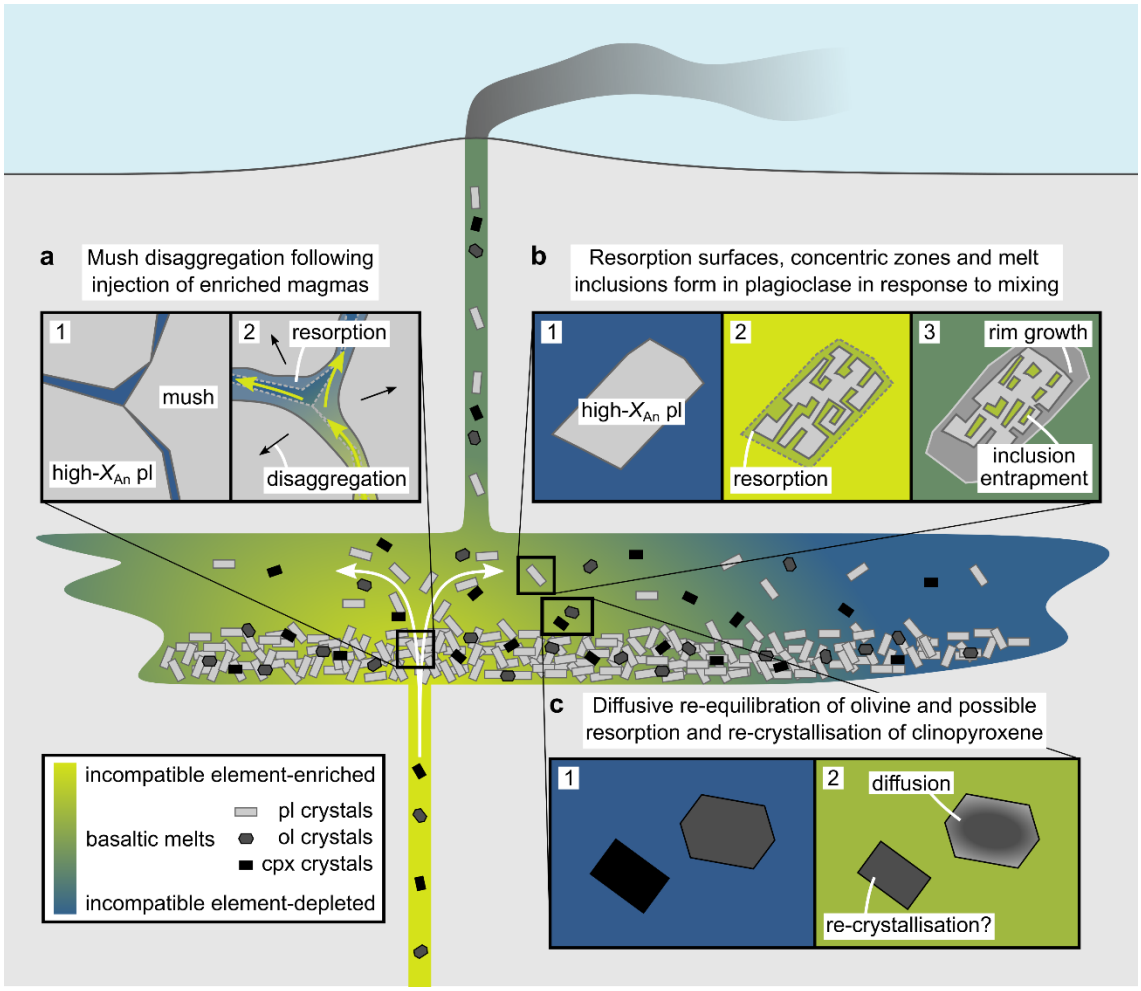

Fig. 10 Cartoon summarising how mixing-induced chemical disequilibrium creates and modifies basaltic crystal cargoes. Primitive and incompatible element-depleted magmas crystallise high-anorthite [high-X_{An}, where X_{An} = Ca/(Ca+Na+K) on a molar basis] plagioclase (pl) alongside olivine (ol) and clinopyroxene (cpx) during storage in the crust[7,70]. Even under isothermal conditions, recharge by incompatible element-enriched and plagioclase-undersaturated primitive magmas can trigger changes in the crystalline portions of incompatible element-depleted and plagioclase-saturated magma reservoirs. **a** The infiltration of plagioclase-dominated mushes by plagioclase-undersaturated liquids may trigger mush disaggregation by triggering resorbing within interstices and along grain boundaries, as indicated by chemical and isotopic disequilibria between some basaltic melts and their cargoes of high-X_{An} plagioclase crystals[22,65]. **b** The transfer of high- X_{An} plagioclase crystals between variably incompatible element-enriched magmas that are also variably saturated in plagioclase produces resorption surfaces, concentric zoning, overgrowth rims and melt inclusions[19,20,23]. **c** Olivine

and clinopyroxene crystals may re-equilibrate, and resorb and re-crystallise, respectively, in response to isothermal mixing of variably incompatible element-enriched magmas with different major element compositions.